The energy injection into waves with a zero group velocity

M. E. Dieckmann, S. C. Chapman, A. Ynnerman, and G. Rowlands

Citation: Physics of Plasmas (1994-present) **6**, 2681 (1999); doi: 10.1063/1.873223
View online: http://dx.doi.org/10.1063/1.873223
View Table of Contents: http://scitation.aip.org/content/aip/journal/pop/6/7?ver=pdfcov
Published by the AIP Publishing

The energy injection into waves with a zero group velocity

M. E. Dieckmann,[a] S. C. Chapman, A. Ynnerman, and G. Rowlands
Space and Astrophysics group, University of Warwick, Coventry, CV 47 AL, United Kingdom

(Received 9 February 1999; accepted 23 March 1999)

The frequency maxima of electron cyclotron harmonic (ECH) waves provide strong responses to sounding in various plasma regimes in the solar system. The frequency maxima correspond to waves for which the group velocity and thus the energy propagation velocity in the plasma frame of reference is zero. A particle-in-cell (PIC) code is employed to show that the propagation of wave energy at a non-zero velocity, necessary to couple energy from a stationary antenna to the plasma, is accomplished by propagating wave precursors. The undamped waves at the frequency maxima of the ECH branches are nonpropagating hence the waves remain localized. It is demonstrated that the nonpropagating waves, built up by the wave precursors, are standing waves. The standing wave generation is followed from the linear to nonlinear regimes. For nonlinear emission amplitudes the emission causes a plasma density depletion close to the antenna. The depletion is shown to trigger a modulational instability in which the ECH wave collapses. The generated nonlinear standing wave also develops an electromagnetic component which couples the electrostatic ECH waves to the fast extraordinary wave. © *1999 American Institute of Physics.* [S1070-664X(99)00707-7]

I. INTRODUCTION

The wave injection into media supporting waves and the properties of the generated wave packets have been investigated in detail in Ref. 1. There it has been shown that the main signal is always preceded by wave forerunners. An interesting case should arise when the group velocity of the generated wave is zero. In this case the main signal cannot propagate. The focus here is on electron cyclotron harmonic (ECH) waves. The linear dispersion relation for these waves has multiple solutions for which the wave group velocity is zero. These particular wave solutions, referred to as the f_q's, are important for plasma sounding experiments.[2] The injection of wave energy and the consecutive sampling of the electric fields at these frequencies gives rise to a strong and long-lasting plasma response to sounding.

We employ the electromagnetic and relativistic particle-in-cell (PIC) code, described in Ref. 3, to investigate the energy transfer into the plasma for these frequencies. The simulations are restricted to one spatial dimension. ECH waves close to the frequency maxima are, in the linear case, electrostatic. Numerical simulations show that this is no longer true once the wave amplitudes reach a nonlinear regime. Then an electromagnetic code is required.

In Sec. II the linear coupling of wave energy from the antenna to the plasma is examined. The linear dispersion relation for undamped ECH waves, propagating perpendicularly to the magnetic field, is solved. This provides the frequency of the f_q as well as the wave group velocities of the ECH wave branch under consideration. The PIC code is then employed to model the emission of a finite wave pulse with its central frequency equal to the f_q. The antenna is modeled by applying forced electric field oscillations to two neighboring simulation grid cells. The emitted wave packet is then analyzed by separating its frequency spectrum into intervals with distinct wave properties. It is shown that the emitted wave packet consists of propagating waves being responsible for the energy transfer to the plasma. The propagating waves generate nonpropagating standing waves with frequencies close to the f_q. These standing waves remain spatially confined. The wave mode responsible for the coupling of wave energy to the f_q is identified.

In Sec. III we compare simulation runs for a range of gradually increasing antenna E fields with the emission frequency and the emission duration kept constant. The plasma response to the emission is followed from the linear to nonlinear regimes. For high emission amplitudes the generated wave perturbation can no longer be described by the linear dispersion relation that was calculated for the initial values of the plasma. Its central wave number is shifted towards lower values which would put the perturbation into a plasma regime supporting only transiently damped waves. The perturbation is, however, weakly damped or undamped.

In Sec. IV the focus is on the nonlinear plasma response at the f_q. The generated perturbation is shown to be a standing wave. Its frequency is broadband, centered at the f_q, and its central wave number is shifted towards lower values of $\tilde{k}$. This shift to low wave numbers is related to an increased plasma temperature at the perturbation's location. The perturbation is shown to collapse when the spatial extent of the plasma density depletion, generated by the emission, matches the wavelength of the f_q. This is a strong indicator that the f_q perturbation collapses by means of a modulational instability. The plasma density depletion is connected with the buildup of currents perpendicular to the ECH wave vector and the background magnetic field. The current system is shown to decrease the magnetic field strength close to the antenna. The perturbation at the f_q gives rise to an oscillatory component of the ambient magnetic field oscillating

[a]Electronic mail: markd@astro.warwick.ac.uk

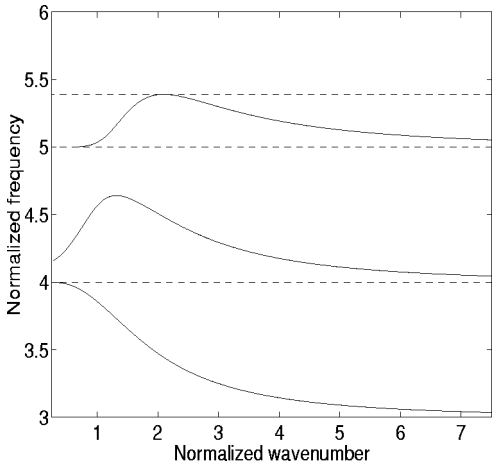

FIG. 1. The undamped solutions of the linear dispersion relation for ECH waves propagating perpendicularly to $\vec{B}$ in the frequency interval $\tilde{\omega}\epsilon$ [3,6]. The two bottom dashed lines are the $n\omega_c$. The uppermost dashed line is the emission frequency. Its intersection point with the ECH wave dispersion relation is the f_q.

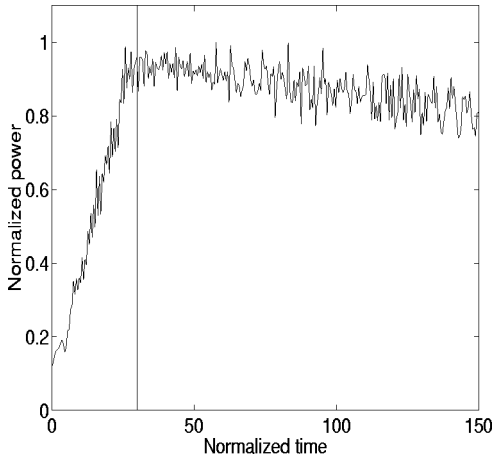

FIG. 2. The electrostatic wave power contained in the simulation box as a function of time. The emission frequency is that of the f_q. The vertical solid line is the emission's end after which the wave power slowly decreases. The weak damping shows that most wave power is concentrated on the undamped ECH wave dispersion relation.

with the f_q's frequency. As a consequence, electromagnetic waves are generated by an electrostatic sounder. The results are discussed with view to the plasma sounding experiment.

II. THE LINEAR PLASMA RESPONSE AT THE F_q

A. The linear dispersion relation

We solve the linear dispersion relation for an electron plasma described by a single Maxwellian velocity distribution. The ambient magnetic field is perpendicular to the wave propagation vector. In this case the plasma supports linearly undamped ECH waves. The electron thermal velocity is $v_{\rm th}$, the electron cyclotron frequency is denoted as ω_c and is set to 10 kHz. The electron plasma frequency is $\omega_p=4\omega_c$. The electron temperature is 2.5 eV. In what follows, all frequencies are normalized to the electron cyclotron frequency and all wave numbers to the inverse electron thermal gyroradius $\omega_c/v_{\rm th}$.

The ECH wave solutions in the interval between $\omega=3\omega_c$ and $\omega=6\omega_c$ are shown in Fig. 1. Overplotted as dashed lines are the harmonics of the cyclotron frequency and the frequency of the f_q that is investigated.

B. The linear antenna-plasma coupling

The employed PIC code uses periodic boundary conditions. The simulation box dimensions are such that no significant wave energy touches the boundaries until the simulation's end. The simulation box consists of 500 grid cells, each with a length of four meters. The electron distribution function is represented by 4608 particles per cell and the proton distribution function is represented by 2312 particles per cell. The antenna is modeled by applying forced electric field oscillations to the simulation cells with the number 250 and 251. The forced oscillations at both cells have an opposite phase. This model corresponds to an antenna that is one dimensional and permeable. The polarization of the forced electric fields is in the simulation direction. The antenna is thus an electrostatic antenna.

The emission duration is 30 wave periods. In what follows, the time t is normalized to one emission wave period T, that is $\tilde{t}=t/T=tf_q$. The f_q is the frequency maximum of the ECH branch found between $5\omega_c$ and $6\omega_c$. The emission amplitude is 0.25 V/m. With a grid cell length of four meters, this corresponds to a peak potential difference of 1 V between the antenna and the surrounding plasma. This is considerably less than, for example, the 80 V peak to peak potential difference between the two antenna plates (i.e., twice the potential between one antenna plate and the surrounding plasma) of the Ulysses sounder.[4]

The wave power, integrated over the wave number interval excited by the emission, is plotted versus the normalized time in Fig. 2. The power is smoothed by averaging over one wave period and it is normalized to the peak power. The vertical solid line indicates the emission's end. One notices an approximately linear increase in the power as a function of $\tilde{t}$ until the emission's end. Then the power gradually drops until the simulation's end.

The simulation did not show any significant wave power at any value of $\tilde{\omega},\tilde{k}$ other than those corresponding to the wave packet. Thus the drop in power cannot be assigned to wave–wave coupling to wave modes which are not part of the emitted wave packet.

Electron trapping can also act as a nonlinear wave damping mechanism. The trapping of particles by ECH waves is described in Ref. 5. The analysis there is, however, valid only for wave frequencies close to a harmonic of ω_c which is not the case for the f_q. The emission amplitude has nevertheless been chosen such as to generate wave packets with amplitudes less than the electric field required to trap electrons if the analysis in Ref. 5 would be valid for the f_q under consideration.

To identify damped wave modes we Fourier transform

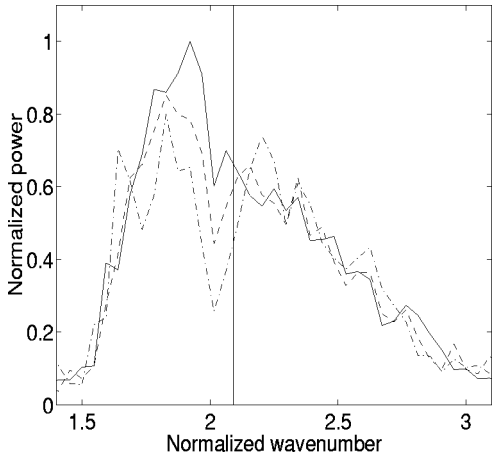

FIG. 3. The electrostatic wave power as a function of $\tilde{k}$ is shown for three simulation time intervals starting at $\tilde{t}=30$ (solid line), $\tilde{t}=85$ (dashed line), and $\tilde{t}=140$ (dash dotted line). The vertical solid line is the f_q. The wave power remains constant (within noise fluctuations) apart from the wave at $\tilde{k}\approx 2$.

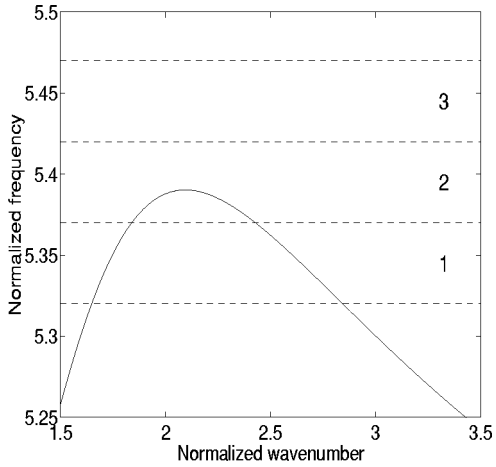

FIG. 4. The solution of the linear dispersion relation for ECH waves propagating perpendicularly to $\vec{B}$ between $5.25\omega_c$ and $5.5\omega_c$. The dashed lines are the boundaries for the three $\tilde{\omega}$ intervals into which the wave packet is split up and examined in Figs. 5–7.

the electrostatic field data (the field component in simulation direction) over space and multiply the result with its complex conjugate. This gives the wave power as a function of $\tilde{k}$ and $\tilde{t}$. The $\tilde{k},\tilde{t}$ spectrum is integrated over 10 emission wave periods each for three different simulation times. The result is shown in Fig. 3. Plotted is the power, normalized to the peak power of the solid curve, versus $\tilde{k}$. The solid curve corresponds to the integration interval $\tilde{t}\ \epsilon\ [30,40]$, i.e., the time immediately after the emission's end. The dashed line corresponds to $\tilde{t}\ \epsilon\ [85,95]$ and the dash dotted line to $\tilde{t}\ \epsilon\ [140,150]$. The vertical solid line shows the wave number of the f_q. The three curves have a similar power for large and for low values of $\tilde{k}$ which shows that the wave modes are undamped. For increasing $\tilde{t}$ the wave power at $\tilde{k}\approx 2$ decreases. This damping is qualitatively different from the damping described in Ref. 5. There we would expect damping of the high $\tilde{k}$ modes.

The distribution of the wave power suggests that the high $\tilde{k}$ modes carry less wave power than the low $\tilde{k}$ modes. This is not necessarily an indicator for wave damping due to trapping. The antenna does not couple equally strong to all wave modes, it couples predominantly to frequencies close to the emission frequency and to high wave numbers (the strong localization in space implies that most power of the antenna electric fields is at high wave numbers).

C. The spatial distribution of the linear wave power

We now look at the power distribution in space of the emitted wave packets. The power is extracted from the electrostatic field data by filtering out specific frequency components. The frequency intervals are shown in Fig. 4. Plotted is $\tilde{\omega}$ versus $\tilde{k}$ of the ECH waves close to the investigated f_q. The interval 1 ($\tilde{\omega}=[5.32,5.37]$) contains waves with a group velocity of $|v_{\rm gr}|=0.1$ or larger. The interval 2 ($\tilde{\omega}=[5.37,5.42]$) contains waves with $|v_{\rm gr}|<0.1$ and the transiently damped waves between the f_q and the upper interval boundary. The interval 3 ($\tilde{\omega}=[5.42,5.47]$) contains no undamped wave solutions of the linear dispersion relation.

To visualize the spatial distribution of the wave power, we apply a Fourier transform over time. We select the bins corresponding to the three frequency intervals shown in Fig. 4. The time integration interval ranges from $\tilde{t}=48$ to $\tilde{t}=150$. The power distribution in the interval 1 is shown in Fig. 5. Plotted is the power, normalized to the peak power, as a function of the grid cell number relative to the antenna position. Two types of power distributions can be found. For a distance of less than 100 grid cells to the antenna the electric field power has pronounced maxima and minima. Since the excited waves have a phase velocity different from zero and since the field power is obtained by integrating over time, the wave perturbation must be a standing wave. The values of the minima do, however, not reach zero which indicates that the perturbation also has propagating wave

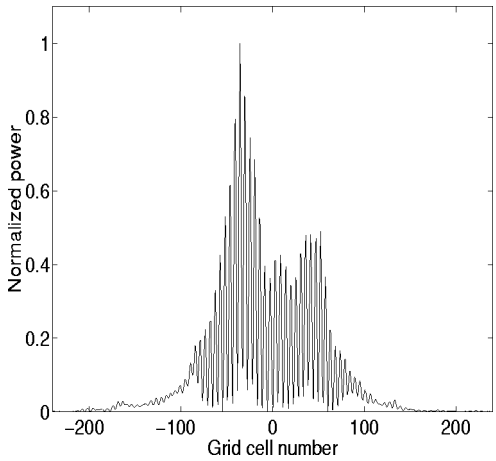

FIG. 5. The power distribution in the interval 1 as a function of the distance (in grid cells) from the antenna. The wave power close to the antenna has pronounced maxima and minima (standing wave). Further away the wave power is a smooth curve (propagating wave).

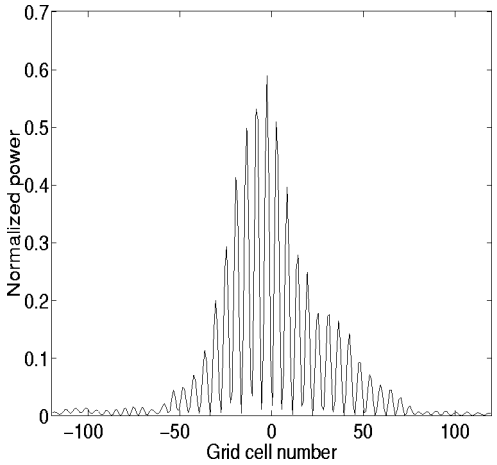

FIG. 6. The power distribution in the interval 2 as a function of the distance (in grid cells) from the antenna. The power distribution shows pronounced maxima and minima (standing wave).

components. For spatial distances from the antenna larger than 100 grid cells the pronounced maxima and minima disappear and are replaced by a smooth curve indicating a propagating wave.

The power distribution for the frequency interval 2 is shown in Fig. 6. Plotted is the power, normalized to the peak power in Fig. 5, versus the grid cell number. Here, the separation into electric field minima and maxima is more pronounced than in the previous plots and here any contribution by propagating waves is absent. The peak power of the central maximum is comparable in intensity to the power maxima in the previous plots.

The power distribution for the interval 3 is shown in Fig. 7. It is normalized to the peak power in Fig. 5 and it is plotted against the grid cell number relative to the antenna. The power levels are lower than those in the previous two plots. This is in agreement with the frequency interval supporting no undamped wave solution of the linear dispersion relation. The spatial extent of the perturbation is approximately the same as the one in Fig. 6.

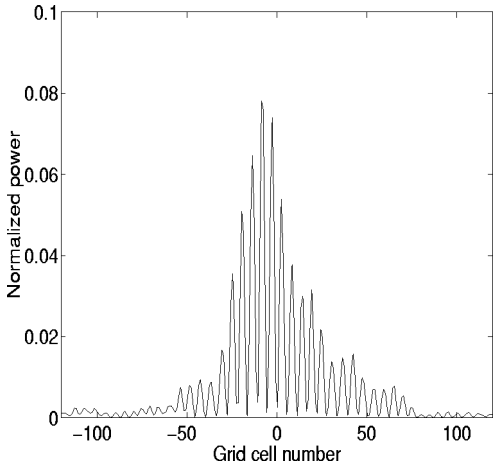

FIG. 7. The power distribution in the interval 3 as a function of the distance (in grid cells) from the antenna. The power distribution shows pronounced maxima and minima (standing wave). The overall power is low (the waves are damped).

From Fig. 5 to Fig. 7 we conclude that the emission at the f_q generates both propagating and nonpropagating waves. The nonpropagating waves can be identified by a pronounced separation of the electric field energy into maxima and minima. The propagating waves were found in the frequency interval 1 whereas the other two frequency intervals contained only nonpropagating waves.

The wave group velocity at $\tilde{\omega}=5.345$, the center of the frequency interval containing the propagating waves, is $v_{\mathrm{gr}} \approx 0.3 v_{\mathrm{th}}$. The time interval between the onset of the sounding and the end of the data window analyzed in Figs. 5–7 is 150 emission wave periods. The grid cell size is 4 meters. Together with the group velocity of the wave mode at the central frequency of the interval 1, which we assume to be representative for this interval, we calculate that the wave front must have propagated a distance $x \approx 200$ grid cells. In Fig. 5 wave forerunners extend up to this distance. They ought to be weak, since they do not reach this distance until the end of the data window. Thus the overall wave power with which they are represented in this window is weak.

In Ref. 1 it has been investigated how waves are built up by a sinusoidal perturbation with a finite duration. The finite emission duration causes a spread of the emission power over a finite frequency range. This causes the generation of wave forerunners with frequencies other than the emission's central frequency. In our case, these forerunners are the waves in the interval containing the propagating waves. If the individual wave components constituting the wave packets have different group velocities they separate. This can be seen from Figs. 5–7. Whereas the waves in Figs. 6 and 7 cover the same spatial range, the waves in Fig. 5 have propagated much further. The arrival of the signal at a given position in Fig. 5 corresponds to a gradual buildup of a wave electric field at this grid cell. According to Ref. 1 this also corresponds to a spread of the wave component's power over a finite frequency interval. This frequency spread covers the nonpropagating f_q. The precursor can thus couple wave energy to the f_q. This coupling then gives rise to the standing waves distributed in space in Figs. 5–7. The buildup of the wave at the f_q is also related to a finite frequency spread of the wave which couples wave power into the interval 3 (Fig. 7). Hence the correlation of the wave power in space between intervals 2 and 3.

The standing waves far from the antenna have been generated by the transfer of wave power from a propagating wave to a nonpropagating wave. The transfer of wave energy between two waves with a different $\tilde{k}$ should reveal the propagating waves involved. The solid line in Fig. 3 indicates that the buildup of the standing wave has been achieved during the wave emission period. The wave power close to the f_q shows no peculiarity. The antenna replaces the power lost by the propagating wave which complicates the identification of the propagating wave responsible for the buildup of the spatially extended standing wave. Figure 7, however, showed that the standing wave has wave components that are transiently damped long (at least 18 emission

wave periods after the emission's end due to the choice of the integration interval) after the emission has finished.

The power lost by the transient damping must now originate from somewhere. Figure 3 reveals that the wave with $\tilde{k}\approx 2$ is damped and the reason has not yet been identified. The group velocity at $\tilde{k}\approx 2$ is $v_{gr}\approx 0.05 v_{th}$. By the end of the simulation this wave should have reached a distance of $x \approx 35$ grid cells away from the antenna. This roughly corresponds to the spatial extent of the standing wave perturbation in Figs. 6 and 7. The $\tilde{k}$ interval in Fig. 4 that supports the damped precursors covers wave numbers with group velocities up to twice the value of $0.05 v_{th}$ which can account for the flanks of the standing wave. The buildup of the standing wave thus seems to be linked to the damping of the propagating waves at $\tilde{k}\approx 2$.

III. THE DEPENDENCE OF THE PLASMA RESPONSE AT THE f_q ON THE EMISSION AMPLITUDE

A series of simulations is performed in which the emission duration and frequency are kept constant while the amplitude is varied. The emission electric fields are: $E_1=0.25$ V/m, $E_2=0.5$ V/m, $E_3=1.0$ V/m, $E_4=2.0$ V/m, $E_5=4.0$ V/m, and $E_6=6.0$ V/m. The highest emission amplitude corresponds to a potential difference of 24 V between the antenna and the surrounding plasma. If the simulation antenna would consist of two plates, as ''real'' sounders do, the peak potential difference between both plates would be 48 V. This potential is still less than, for example, the sounder onboard the Ulysses experiment applies between its plates.[4]

Six simulations using the electric field amplitudes have been performed. The plasma parameters were as in the simulation in the preceding Section. The number of particles per cell are, however, reduced by a factor of 4 for both the electron and the proton species.

The electrostatic field data, i.e., the electric field in simulation direction, between $\tilde{t}=30$ and $\tilde{t}=150$ is Fourier transformed in space and time.

In Fig. 8(a)–8(f), the power as a function of $\tilde{\omega},\tilde{k}$ is shown for the six emission amplitudes E_1 to E_6. Plotted is the normalized frequency versus the normalized wave number. The power is plotted on a $\log_e$ scale with the power being normalized to the peak power in Fig. 8(f). Overplotted as a solid line is the solution of the linear dispersion relation. The dashed line shows $\tilde{\omega}=5$.

Fig. 8(a) shows the case of an emission amplitude of E_1 which is the same emission amplitude as for the simulation described in the preceding Section. The antenna has spread wave energy over a large $\tilde{k}$ interval along the solution of the linear dispersion relation. The frequency of the wave energy is close to the emission frequency of $\tilde{\omega}\approx 5.4$. The f_q carries significant wave energy.

Figure 8(b) represents the emission amplitude E_2. The wave power is concentrated at the wave numbers $\tilde{k}\approx 1.7$ and $\tilde{k}\approx 2.3$. The simulation solution of the dispersion relation matches the solution of the linear dispersion relation. The concentration of wave power at the higher wave number indicates that particle trapping does not yet absorb significant wave energy. The power at the f_q is at a local minimum which is, however, still large compared to the noise levels. The noise levels are lower than the values shown on the colorbar. The noise is distributed over the simulation box whereas the signal is concentrated near the antenna. Thus the signal power, if present, is large compared to the noise.

Figure 8(c) shows the dispersion relation for the simulation with E_3. The increased emission amplitude did not increase the power of the ECH waves propagating on the undamped solution of the linear dispersion relation, indeed the power of the ECH wave at $\tilde{k}\approx 2.3$ is found to decrease. At the same time the wave power placed on the transiently damped wave solutions close to the ECH branch has increased relative to the power placed on the linearly undamped ECH branch. This indicates a nonlinear damping mechanism acting on the waves propagating on the linearly undamped ECH wave branch with the damping being stronger for the ECH wave at high $\tilde{k}$. The property of the damping mechanism of being $\tilde{k}$ selective is what we would expect from nonlinear Landau damping due to trapping.[5] The analysis in Ref. 5 would, however, predict that the maximum power supported by the ECH wave branch does remain constant once the nonlinear saturation wave amplitude is reached. This does not agree with the observed decrease of the wave power at $\tilde{k}\approx 2.3$. In Ref. 5 trapping by a monochromatic wave close to a harmonic of the cyclotron frequency has been investigated. Here we excite two ECH wave packets with frequencies in between two harmonics of ω_c. In addition the absorbed wave energy heats the plasma changing the linear dispersion of the ECH wave modes close to the antenna. The trapping characteristics may thus differ.

In Fig. 8(d) the dispersion relation for an emission amplitude of E_4 is shown. The power peak at $\tilde{k}\approx 2.3$ has now been replaced by a continuous distribution with a low power level over a wide frequency range. The power peak at $\tilde{k}\approx 1.7$ has not increased in overall power but is now spread over a large $\tilde{k}$ range. The reason for the spread in $\tilde{k}$ is examined in Sec. IV for an emission frequency of E_6. There it is shown that the spread is partially due to a shift in $\tilde{k}$ of the frequency maximum in time and it is partially caused by a spread in $\tilde{k}$ of the wave perturbation.

Figure 8(e) corresponds to the emission amplitude E_5. The power peak at low $\tilde{k}$ has been shifted towards even lower values than for E_4. The main peak is now decoupled from the solution of the linear dispersion relation. At the same time a new power peak emerged at $\tilde{k}\approx 2$ but at a higher $\tilde{\omega}$ than the linear dispersion relation would suggest.

Figure 8(f) shows the simulation dispersion relation for an emission amplitude E_6. The main power peak is located at $\tilde{k}\approx 1.1$. The second power peak is propagating on the linear dispersion relation solution at $\tilde{k}\approx 1.7$.

IV. THE NONLINEAR PLASMA RESPONSE AT THE F_q

The electrostatic field perturbation produced by an emission amplitude E_6 is shown in Fig. 9. Plotted is the logarithmic power, normalized to the peak power, as a function of

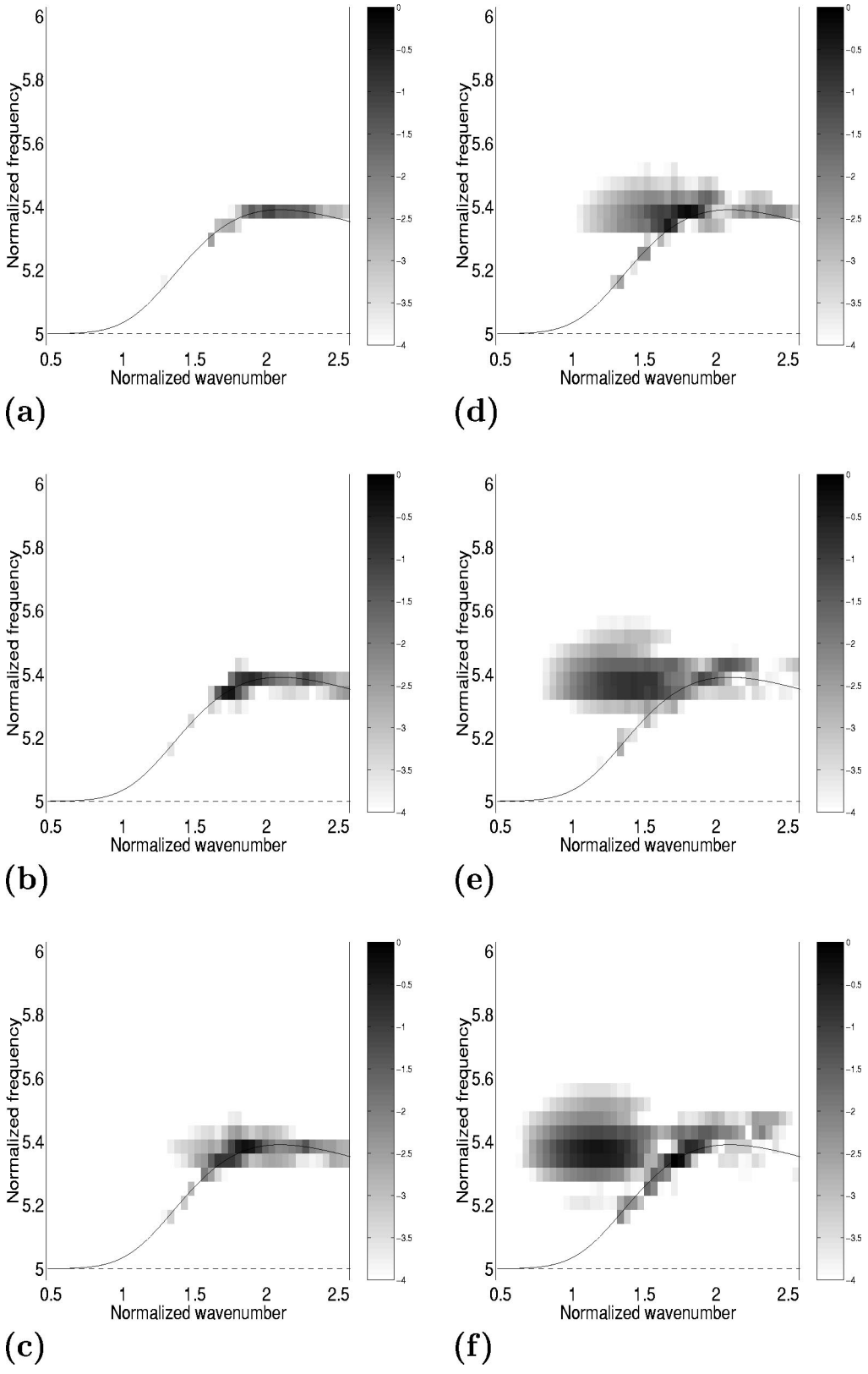

FIG. 8. (a)–(f) show the simulation dispersion relations for the excited ECH waves for the emission amplitudes E_1 (a) to E_6 (f). For increasing emission amplitudes the wave packet splits in $\tilde{k}$ close to the f_q. The low $\tilde{k}$ component moves towards lower $\tilde{k}$ for increasing emission amplitudes.

the simulation grid cell number relative to the antenna's position and the normalized time. The emission ends at a time $\tilde{t}=30$. For visualization purposes, the electric fields at the two antenna grid cells in the plot are set to zero during the emission. The perturbation shows the pronounced power maxima and minima typical for a standing wave. At $\tilde{t}\approx 70$ the perturbation collapses and waves can be seen propagating away from the flanks of the perturbation.

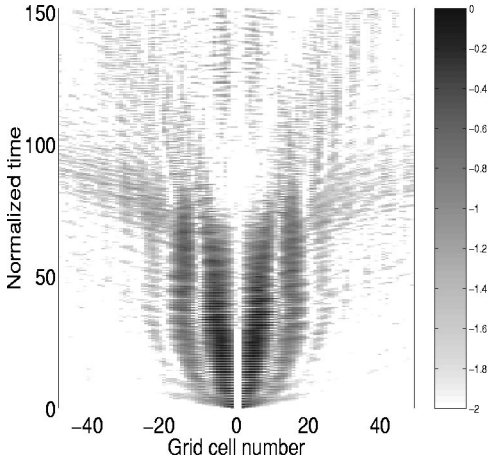

FIG. 9. The logarithmic power of the squared electrostatic field. The emission (up to $\tilde{t}=30$ with the amplitude E_6) generates a wave perturbation which then collapses at $\tilde{t}\approx 70$.

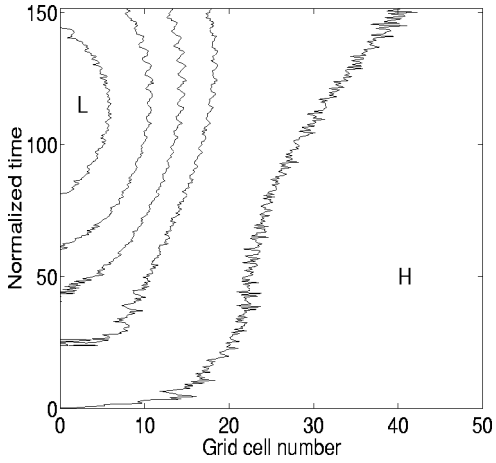

FIG. 11. The $\vec{B}$ field strength. The contour lines correspond to 0.9996 to 1.0000 in steps of 0.0001 from L to H. The emission process and the perturbation in Fig. 9 reduces the $\vec{B}$ field strength at the antenna. The fields get stronger after the perturbation's collapse.

By Fourier transforming the electrostatic field data in space and multiplying the result with its complex conjugate, one obtains the power as a function of $\tilde{k},\tilde{t}$. The electric fields at the two antenna grid cells during the emission are set to zero to improve the dynamical range in Fig. 10. The logarithmic power is plotted versus the normalized wave number and the normalized time. The power is normalized to the peak power. Up to $\tilde{t}=30$ the antenna is pumping energy into the plasma, in particular at high wave numbers. The antenna excites the ECH mode at $\tilde{k}\approx 1.5$ and, while the wave power increases and the time proceeds, the central wave number of the wave shifts to lower values of $\tilde{k}$. At $\tilde{t}\approx 70$ the structure at low $\tilde{k}$ collapses and a wave at $\tilde{k}\approx 1.9$ emerges. While the perturbation at $\tilde{k}\approx 1.2$ can be associated with the power peak at the same wave number in Fig. 8(f), the power peak at $\tilde{k}\approx 1.9$ corresponds to the wave propagating on the undamped ECH branch in the same figure. Figure 9 indicates that the linear wave is generated at the flanks of the nonlinear perturbation, i.e., where the plasma has not been strongly affected by the emission.

During the emission the electron temperature perpendicular to the magnetic field direction increased. For an emission amplitude E_1 it increased by 0.2 percent, whereas it increased by 15 percent for E_6. Since the simulation direction is perpendicular to the magnetic field, the electrons are spatially confined. The increase in the kinetic energy is thus related to an increase of the particle temperature close to the antenna. The wavelength of the ECH waves is linked to the electron thermal gyroradius. It is shown below that the change in ω_c during the simulation is of the order of 10^{-4} of the initial value. It is thus negligible compared to the increase in v_{th} for an emission amplitude E_6. The simulation box size is fixed and the wave numbers are thus given in physical units. Figs. 8(a)–8(f) are plotted in normalized wave numbers using the electron's v_{th} from before the emission. The physical wave number is related to the normalized wave number by $k=\tilde{k}\omega_c/v_{\mathrm{th}}$ with $\tilde{k}$ being independent of the temperature. Increasing v_{th} will thus shift the physical wave number towards lower values. This causes the central wave number of the perturbation in Fig. 9 to move towards lower values. The perturbation's collapse then generates waves in the surrounding plasma where the electron's thermal velocity has not been increased. These waves propagate on the undamped ECH branch in Fig. 8(f).

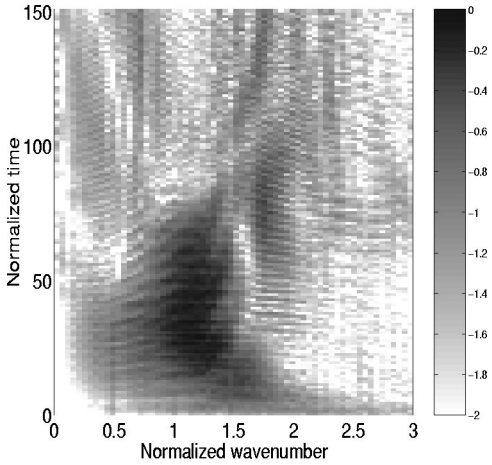

FIG. 10. The logarithmic power spectrum of the field perturbation shown in Fig. 9. The high emission amplitude shifts the $\tilde{k}$ of the perturbation towards lower values (due to electron heating). The low $\tilde{k}$ perturbation collapses at $\tilde{t}\approx 70$.

In Fig. 11 the response of the background magnetic field (i.e., the component perpendicular to the simulation direction) to the emission is shown. Plotted is the magnetic field strength, normalized to its initial average value, versus the grid cell number relative to the antenna and versus $\tilde{t}$. The antenna is located at cell 0. The contour lines denote values of 0.9996–1.0000 in steps of 10^{-4} with the lowest magnetic field strength indicated by an L and the highest magnetic field indicated by an H. The minimum field is 0.9994 and the maximum is 1.0001. After the emission has started at $\tilde{t}=0$ the contour line 1.0000 rapidly moves towards large dis-

tances from the sounder. The time over which the magnetic field is pushed out is of the order of an electron cyclotron period. The demagnetization slows down at a distance of approximately 20 grid cells which corresponds to the electron gyroradius of a particle with $v \approx 5 v_{\mathrm{th}}$. This is the maximum velocity up to which electrons were initialized in the simulation. The velocity with which the magnetic field perturbation propagates into the plasma and the maximum distance it reaches before its velocity decreases indicates that the early magnetic field perturbation is propagated by electrons.

After the emission stopped, the magnetic field close to the antenna further diminishes until $\tilde{t} \approx 70$, which correlates well with the collapse of the nonlinear wave perturbation at the f_q shown in Fig. 9. At even later times the magnetic field at the antenna recovers in strength while the contour line 1.0000 propagates into the plasma with a slow and almost constant velocity. The propagation velocity is approximately twice the thermal velocity of the protons. The times over which the magnetic field recovers as well as the propagation velocity at the time $\tilde{t} > 70$ indicates that the late time evolution of the magnetic field is governed by the protons.

If the magnetic field perturbation at later stages would be governed by the protons, the proton kinetic energy should reflect this. For the case of an emission amplitude E_1 the proton kinetic energy initially drops (not shown) by $2 \cdot 10^{-4}$ times the initial energy and then fluctuates by one fourth times that value. The simulation electric fields are initialized as zero. The protons are initialized such as to give a statistical representation of a Maxwellian velocity distribution. The statistical nature of the particle velocity distribution causes noise electric fields to build up. The electric field energy is taken from the proton kinetic energy and thus the proton energy is diminished.

For an emission amplitude E_6 the proton kinetic energy also drops initially but then increases by $8 \cdot 10^{-3}$ times the initial energy. After having reached its maximum the energy starts to oscillate.

The temporal change in the magnetic field could generate electromagnetic waves. The magnetic field component parallel to the background magnetic field as a function of x,t minus its mean value is Fourier transformed in time. The result shows the spatial distribution of transverse magnetic (TM) electromagnetic waves with a frequency $\tilde{\omega}$. We now focus on low frequency waves (which are related to the magnetic field evolution governed by the protons) and on high frequency waves (which are related to the emission process and to the fast initial evolution of the ambient magnetic field).

The spatial distribution for the low frequency waves is shown in Fig. 12. Plotted are contour lines for the normalized power versus the grid cell number relative to the antenna and versus the normalized frequency. The plasma is homogeneous and the antenna electric field is symmetric. The power distribution is thus symmetric to the antenna. The power for grid cells equally far away from the antenna's center has been summed up to improve the signal to noise ratio. The values for the contour lines of the logarithmic

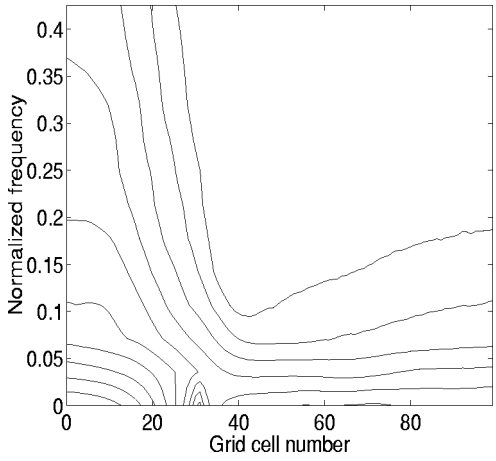

FIG. 12. The low $\tilde{\omega}$ component of the Fourier transform in time of $\vec{B} - \langle \vec{B} \rangle$. The contour lines show values of the logarithmic power from -5 to -0.5 in steps of 0.5. Wave activity at low $\tilde{\omega}$ close to the antenna indicates a proton reaction to the emission.

power, normalized to the peak power, range from -5 to -0.5 in steps of 0.5. The wave power peaks at low frequencies and at two points. One is close to the antenna and the second is at relatively large distances from the antenna. At cell 30 the power drops, at low frequencies, by several orders of magnitude.

At distances of less than 30 grid cells away from the antenna the contour lines show strong wave activity over the entire frequency interval. At a distance of approximately 40 grid cells away from the antenna, the power distribution falls off quickly as a function of frequency. For distances increasing further, the low frequency noise converges to the power distribution of the unperturbed plasma. The Fourier transform has been applied to an expanding magnetic field structure. It is thus not useful to try to relate the strong noise power gradient at a distance of 40 grid cells to any physical quantity. The power dropping off at cell 30 and at $\tilde{\omega} = 0$ indicates that the initial magnetic field compression counterbalances the consecutive magnetic field depression (The fast Fourier transform (FFT) at $\tilde{\omega} = 0$ corresponds to a sum over the individual field values at one grid cell in time).

The power distribution for the high frequency waves is shown in Fig. 13. Plotted is the power, normalized to the peak power in Fig. 12, versus the grid cell number and versus $\tilde{\omega}$. The contour lines for the logarithmic power are -5.5, -4.9, and -4.3. The power increases from the outside to the inside of the structures visible at $\tilde{\omega} \approx 5.4$ where it peaks. The magnetic field is modulated by the strong electric fields of the wave perturbation at the $\tilde{\omega} \approx 5.4$. This modulation can, in principle, generate fast extraordinary wave modes. The magnetic field perturbation is localized and has thus a spread in $\tilde{k}$. The f_q perturbation oscillates with a frequency that is also an undamped frequency of the fast extraordinary mode. The components of the f_q perturbation with $\tilde{k}, \tilde{\omega}$ matching the values for the fast extraordinary mode could then be propagated away.

That this is the case is shown in Fig. 14. The upper curve shows the electrostatic field energy, normalized to its peak

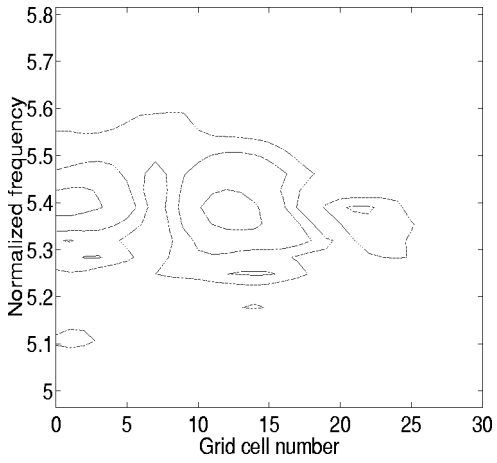

FIG. 13. The high $\tilde{\omega}$ component of the Fourier transform in time of $\vec{B}-\langle\vec{B}\rangle$. The contour lines show the values of the logarithmic power of -5.5, -4.9, and -4.3. Wave activity at the emission frequency indicates that the strong electrostatic fields modulate the $\vec{B}$ field.

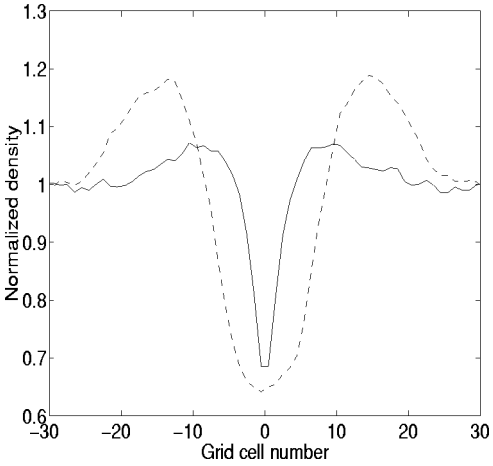

FIG. 15. The solid curve shows the electron density distribution at $\tilde{t}\approx 30$. The dashed line shows it for $\tilde{t}\approx 70$ when the wave perturbation collapses. The electron density is reduced by the wave. The depletion propagates into the plasma at a lesser speed than the fields (Fig. 9).

value, versus the normalized time. Up to $\tilde{t}=30$ most of the field energy is linked to the antenna electric fields. Then the energy drops by one order of magnitude. At this stage most electrostatic field energy is contained in the perturbation at the f_q. This perturbation then collapses at $\tilde{t}\approx 70$ to be replaced by the noise fluctuations.

The lowest curve shows the energy contained in the electric field component perpendicular to both the background magnetic field and the simulation direction, and is thus linked to the fast extraordinary waves. The curve is normalized to the peak value of the upper curve. Up to $\tilde{t}\approx 40$ the energy is down to noise levels. Then the energy grows to reach its final level at $\tilde{t}\approx 60$. The beat indicates that the fast extraordinary wave has been excited over a wide frequency range. The waves grow after the emission has finished and before the wave collapses, i.e., during the time when the high frequency modulations of the background magnetic field are strongest. The middle curve is the sum of the lower curve and the magnetic field energy minus its initial value. It thus shows the energy contained in the magnetic field oscillations and the electromagnetic waves. No substantial increase in the energy can be linked to the growth of the lower curve. This shows that most energy is stored in the oscillations and only a small fraction is coupled into the fast extraordinary mode. This may have been expected since the wave number of the f_q perturbation strongly differs from the wave numbers of the low frequency part of the fast extraordinary mode. The overall increase in the electromagnetic field energy is small compared to the decrease in the electrostatic field energy. The collapse of the f_q perturbation is thus not related to the electromagnetic instability. The coupling to propagating linear electromagnetic waves could, for different plasma parameters, be a saturation mechanism for the electrostatic perturbation at the f_q.

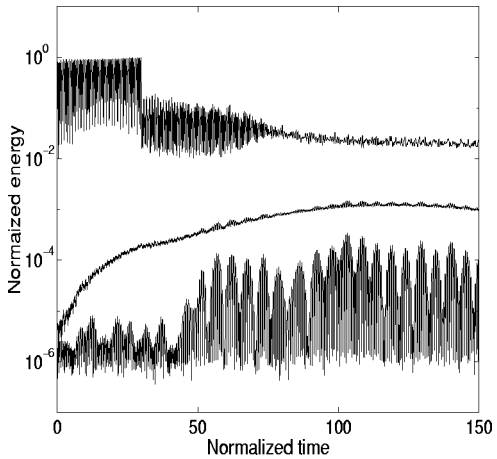

FIG. 14. The three curves are the electrostatic field energy (upper curve), the electromagnetic wave field energy (middle curve) and the energy of the electromagnetic wave electric field component (lower curve). Most wave energy is contained in the electrostatic fields. The increase in the electromagnetic energy reflects the $\vec{B}$ field modulation by the emission whereas the lowest curve shows wave coupling from electrostatic into slow extraordinary mode waves.

So far the reason for the sudden collapse of the wave perturbation at the f_q has not been identified. The magnetic field depletion is weak, so one would assume that it is not the trigger for the wave collapse. The particle kinetic energies are, for an emission amplitude E_6, strongly affected by the emission and by the perturbation. The collapse of the perturbation may thus be related to a particle property. In Fig. 15 the electron density profiles for two simulation times are compared. The densities are integrated from $\tilde{t}=20$ to $\tilde{t}=30$ (solid line) and from $\tilde{t}=60$ to $\tilde{t}=70$ (dashed line). The density is then normalized to the density averaged over the simulation box and plotted versus the grid cell number relative to the antenna. Both curves show a significant electron density depletion close to the antenna and an increase in the electron density away from the antenna. The values of the density minima for both curves are comparable. The dashed curve shows a minimum extending over a larger spatial interval at later $\tilde{t}$. This shows that the density perturbation is expanding even after the emission's end. The expansion is

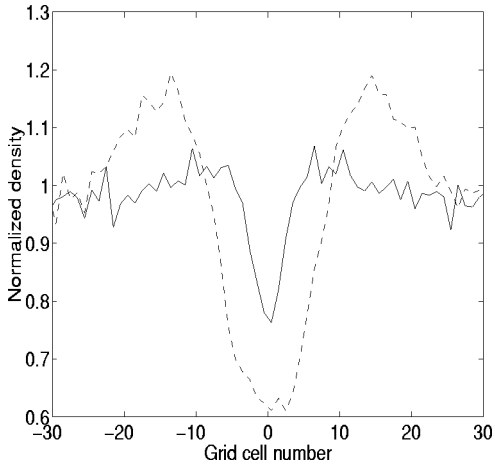

FIG. 16. The solid curve shows the proton density distribution at $\tilde{t} \approx 30$. The dashed line shows it for $\tilde{t} \approx 70$. The protons react to the wave perturbation which explains the wave activity at low $\tilde{\omega}$ in Fig. 12.

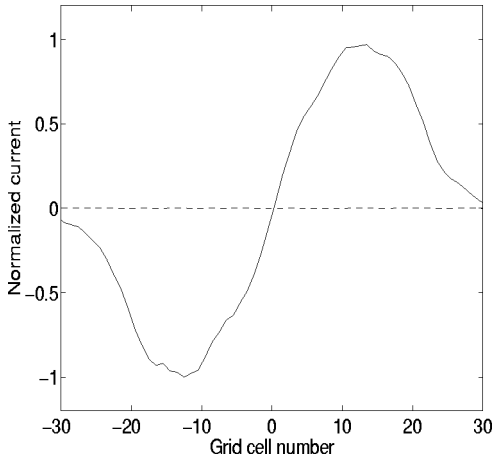

FIG. 17. The electron current (solid line) and the proton current (dashed line) perpendicular to both the simulation direction and $\vec{B}$. The $\vec{B}$ field distribution is upheld by the electron current.

also slower than the expansion of the electric fields into the plasma. The electrostatic field perturbation at the f_q reaches its maximum extent of 40 grid cells at the emission's end (compare Fig. 9) whereas, at this time, the electron density perturbation has spread over approximately 20 grid cells (compare Fig. 15).

The proton density profiles are shown in Fig. 16. The curves correspond to the same integration intervals as the curves in Fig. 15. The density minimum for the solid line is less pronounced both in its width and in its minimum value. As we might expect, the protons react more slowly than the electrons to the emission.

The density profiles for the dashed lines in Figs. 15 and 16 are comparable. In both cases the density is the average value at a distance of approximately 10 grid cells away from the antenna.

The ambient magnetic field at the antenna has been depressed by the emission. The magnetic field decrease must be related to a current in the plasma. The magnetic field evolution is slow thus the current should not oscillate quickly. In simulation direction the emission generated an oscillating electric field perturbation. This perturbation involves electron and proton waves. The bulk magnetic field evolution shows weak oscillations at ECH wave frequencies but the main part evolves on a time scale that is slower than the proton current oscillations. No electron or proton currents apart from noise fluctuations can be detected in the direction of the background magnetic field. In Fig. 17 the currents, perpendicular to the ambient magnetic field and the simulation direction, are shown for the electron species (solid line) and the protons (dashed line). The currents are integrated over the time (after the sounding interval) $\tilde{t}=60$ to $\tilde{t}=70$ and are normalized to the maximum value of the solid line. The currents are plotted versus the grid cell number relative to the antenna. The proton current is negligible whereas the electron current correlates with the magnetic field profile in Fig. 11. There, the contour line 1.0000 at the time $\tilde{t} \approx 70$ is at a distance of 30 grid cells away from the antenna. The electron current in Fig. 17 goes to noise levels at this value. The emission generates two electron beams supporting the magnetic field depletion. The electron beams are in an almost steady state. Thus the magnetic field depression is related to a gradient drift current, i.e., $dB_y/dx = J_z$ if the background magnetic field is oriented in the y direction and if the simulation direction is the x direction.

In Fig. 18 the electrostatic wave power as a function of the grid cell number is shown. The wave power is integrated over the time $\tilde{t}=60$ to $\tilde{t}=70$ which is the time immediately preceding the collapse of the wave perturbation. The time integrated wave power shows again the minima and maxima characteristic for a standing wave. The first power minima at this simulation time are located at a distance of 10 grid cells away from the antenna. The particle density first recovers to the (normalized) background value in Figs. 15 and 16 at the same locations. The wavelength of the waves involved in the standing wave (see Fig. 9) is 20 grid cells (since it is a standing wave the wavelength of the waves involved is the distance between every second power minimum). This matches the dimension of the plasma density depletion at the

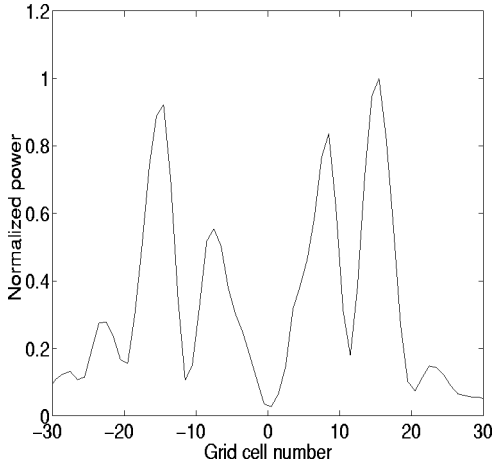

FIG. 18. The wave power of the f_q perturbation at $\tilde{t} \approx 70$. The wave perturbation collapses when the electron and proton density depletions in Figs. 15 and 16 evolve to a spatial extent similar to the perturbation's wavelength.

time of the collapse. Figure 9 also shows that the perturbation collapses from the inside to the outside, i.e., where the density depletion is largest. The timing of the collapse and the spatial decay of the perturbation strongly suggest that the mechanism responsible for the collapse is a modulational instability.

V. DISCUSSION

In this work the coupling between an antenna and the surrounding plasma has been investigated. The antenna model corresponds to a one dimensional permeable and electrostatic antenna. The plasma is collisionless with one electron and one proton species, each with a single Maxwellian velocity distribution. The emissions have been restricted to a wave propagation direction perpendicular to the background magnetic field exciting only undamped ECH waves.

It has been shown that the antenna can couple energy to wave modes with a group velocity (and thus an energy propagation velocity) of zero via non-zero group velocity forerunners. The generation of wave forerunners by sinusoidal emissions with a finite duration has been discussed in detail in Ref. 1. In this work, the presence of wave forerunners has been confirmed by means of numerical PIC simulations and indications have been given that they are responsible for the buildup of the plasma perturbation at the f_q. The wave, if nonpropagating, is a standing wave. This observation may be explained in terms of the coupling mechanism. The forerunner's wave front has a spread in frequency covering the f_q which it excites. The wave front encounters an unperturbed plasma without any current modulations related to the wave front's electric field. The electric field must then consist of two waves with equal frequency and opposite phase velocities which are related to two equally strong currents with opposite sign. The currents cancel out to zero. The two waves are linearly undamped and form the standing wave observed.

The decay of a wave with a slow group velocity has been related to the transient damping of the wave perturbation with a frequency higher than the f_q, a frequency that is not an undamped solution of the linear dispersion relation.

The wave buildup at an f_q has been investigated for wave electric field strengths ranging from a linear to a strongly nonlinear regime. It has been shown that the main nonlinear modification to the plasma perturbation is a downwards shift in its wave number. This has been explained in terms of an electron temperature close to the antenna that increases with increasing emission amplitudes. The widening of the wave number spectrum may be related to the spatially inhomogeneous electron temperature and density profile.

For emission amplitudes in the nonlinear regime the magnetic field is modified by the strong wave electric fields. The onset of the emission creates a magnetic field depletion which is propagated into the unperturbed plasma first by electrons and, once the perturbation crosses a distance of more than the electron gyroradius of the fastest electrons, by protons. The depletion has been linked to an electron current system built up by the emission. The magnetic field also experiences a modulation at the ECH wave frequency. For sufficiently strong perturbation electric fields, the magnetic field oscillations can generate fast extraordinary mode waves.

The emission also produced a plasma density depletion for both the electrons and the protons. The density depletion propagates into the plasma more slowly than the electrostatic field perturbation. Once the depletion size becomes comparable to the wavelength of the f_q perturbation, the f_q wave collapses by means of a modulational instability.

Some of the properties of the wave perturbation may be generalized to three dimensions. The predicted properties may then be compared to the wave response spectrum given by a plasma sounder. The electron heating due to electron trapping is dependent on the electric field. The large potential differences between the antenna plates of a plasma sounder are expected to heat the electrons causing a depletion of the plasma density. The overall heating may, however, not be as effective as in the one dimensional case because in a real plasma particles are free to move along the magnetic field lines thus refreshing the plasma pool. At the same time the hot electrons can propagate out of the antenna's vicinity. The plasma would then react linearly to the wave perturbation at the f_q up to higher ECH field values and thus emission amplitudes. The wave perturbation would then be stable. Long-lasting responses to sounding at the f_q's have been observed, for example, in the plasma trough.[2] The plasma response duration can be up to 300 ms. A typical frequency of an f_q in the plasma trough would be around 20 kHz. The response duration would then be several thousand f_q wave cycles as compared to a stable f_q perturbation of several ten wave cycles for the simulation with an emission amplitude of E_6.

Interestingly, the f_q's are rarely observed in the Ionosphere.[2] Their absence might be related to the modulational instability. The Debye length and the electron thermal gyroradius in the Ionosphere are small compared to the antenna dimensions. The characteristic distance over which the particles can move along the magnetic field lines during the emission may thus be small compared to the dimensions of the wave perturbation. In this case the f_q perturbation would be more similar to the one dimensional case than, for example, in magnetospheric plasmas. The collapse of the f_q's may thus be more relevant for ionospheric plasmas than it is for magnetospheric plasmas.

A spacecraft moving relative to the plasma frame of reference, i.e., the frame of reference of the waves involved in the perturbation, should see a Doppler shift of the waves. Waves with opposite phase velocities would experience a Doppler shift in their frequency with an opposite sign. The plasma response picked up by the antenna would then show two peaks instead of one. The phase velocities of the f_q's are low. For the plasma considered ($\omega_c = 10$ kHz, $\omega_p = 4\omega_c$, $v_{\mathrm{th}} = 9.4 \cdot 10^5$ m/s, $f_q = 5.4\omega_c$) it is $v_{\mathrm{ph}} \approx 2.5 \cdot 10^6$ m/s. The values of ω, ω_p, and ω_c employed by the simulation are realistic for magnetospheric plasmas encountered, for example, by the GEOS mission (compare Fig. 2 in Ref. 2). Typical velocities for the GEOS and ISEE (International Sun-Earth Explorer) sounders in the plasma frame of reference are given in Ref. 4 with $v_{\mathrm{rel}} = 0.005 v_{\mathrm{th}}$. The frequency

gap $\Delta\tilde{\omega}$ between the two peaks at the f_q due to the Doppler shift is given by $|\Delta\tilde{\omega}|=2\tilde{k}v_{\mathrm{rel}}/v_{\mathrm{th}}$. The factor of 2 arises from the f_q's with opposite phase velocities being Doppler shifted in opposite frequency directions. Note that, for purely electrostatic ECH waves, the Doppler shift does depend only on the relative value $v_{\mathrm{rel}}/v_{\mathrm{th}}$. For the f_q under consideration $\tilde{k}=2$. Thus $|\Delta\tilde{\omega}|=0.02$ and $|\Delta\omega|=200$ Hz for the simulation ω_c which should be detectable. In Ref. 2 it has been stated that the response at the f_q's indeed split up into two resonances, separated by a few hundred Hz and the splitting has been explained by nonMaxwellian electron velocity distributions. The splitting of the resonances due to a Doppler shift is an alternative explanation to that in Ref. 2 but it has not been shown in this work if it is still the f_q's providing the plasma response if the satellite moves relative to the plasma. Future work thus has to include a relative motion between the simulation plasma and the emitting antenna.

ACKNOWLEDGMENTS

Mark Dieckmann has been funded throughout this work by the University of Warwick, by the CNRS Orléans and by the European network grant FMRX-CT98-0168. The authors would like to thank V. V. Krasnosel'skikh and P. M. E. Décréau for the discussions contributing to this work as well as the Swedish National Supercomputer Center at Linkoeping for the generous provision of computer time on its Cray T3E.

[1] L. Brillouin, *Wave propagation and group velocity* (Academic, London, 1960), Chaps. 4.6 and 4.7.
[2] J. Etcheto, H. de Feraudy, and J. G. Trotignon, Adv. Space Res. **1**, 183 (1981).
[3] P. E. Devine, S. C. Chapman, and J. W. Eastwood, J. Geophys. Res. **100**, 17189 (1995).
[4] P. Le Sager, Patrick Canu, and Nicole Cornilleau-Wehrlin, J. Geophys. Res. **103**, 26667 (1998).
[5] S. Riyopoulos, J. Plasma Phys. **36**, 111 (1985).
[6] W. Baumjohann and R. A. Treumann, *Basic Space Plasma Physics* (Imperial College Press, London, 1996), p. 7.